NEMA NU 1-2018 performance characterization and Monte Carlo model validation of the Cubresa Spark SiPM-based preclinical SPECT scanner

Matthew Evan Strugari (✉ matthew.strugari@dal.ca)

Dalhousie University   https://orcid.org/0000-0001-8045-9126

Drew Roderick DeBay

Cubresa Inc

Steven Donald Beyea

Dalhousie University Department of Physics and Atmospheric Science

Kimberly Dawn Brewer

Dalhousie University Department of Physics and Atmospheric Science

---

Original research

NEMA NU 1-2018 performance characterization and Monte Carlo model validation of the Cubresa Spark SiPM-based preclinical SPECT scanner

Matthew E. Strugari[1,2*], Drew R. DeBay[1,3], Steven D. Beyea[1,2,4,5] and Kimberly D. Brewer[1,2,4,5,6]

*Correspondence:
matthew.strugari@dal.ca
[1]Biomedical Translational Imaging Centre, Halifax, NS, Canada
Full list of author information is available at the end of the article

Abstract

Background: The Cubresa Spark is a novel benchtop silicon-photomultiplier (SiPM)-based preclinical SPECT system. SiPMs in SPECT significantly improve resolution and reduce detector size compared to preclinical cameras with photomultiplier tubes requiring highly magnifying collimators. The NEMA NU 1 Standard for Performance Measurements of Gamma Cameras provides methods that can be readily applied or extended to characterize preclinical cameras with minor modifications. The primary objective of this study is to characterize the Spark according to the NEMA NU 1-2018 standard to gain insight into its nuclear medicine imaging capabilities. The secondary objective is to validate a GATE Monte Carlo simulation model of the Spark for use in preclinical SPECT studies.

Methods: NEMA NU 1-2018 guidelines were applied to characterize the Spark's intrinsic, system, and tomographic performance with single- and multi-pinhole collimators. Phantoms were fabricated according to NEMA specifications with deviations involving high-resolution modifications. GATE was utilized to model the detector head with the single-pinhole collimator, and NEMA measurements were employed to tune and validate the model. Single-pinhole and multi-pinhole SPECT data were reconstructed with the Software for Tomographic Image Reconstruction and HiSPECT, respectively.

Results: The limiting intrinsic resolution was measured as 0.85 mm owing to a high-resolution SiPM-array combined with a 3 mm-thick scintillator. The average limiting tomographic resolution was 1.37 mm and 1.19 mm for the single- and multi-pinhole collimators, respectively, which have magnification factors near unity at the center of rotation. The maximum observed count rate was 15,400 cps, and planar sensitivities of 34 cps/MBq and 150 cps/MBq were measured at the center of rotation for the single- and multi-pinhole collimators, respectively. All simulated tests agreed well with measurement, where the most considerable deviations were below 7%.

Conclusions: NEMA NU 1-2018 standards determined that a SiPM detector mitigates the need for highly magnifying pinhole collimators while preserving detailed information in projection images. Measured and simulated NEMA results were highly comparable with differences on the order of a few percent, confirming simulation accuracy and validating the GATE model. The multi-pinhole collimator investigated in this study offers the optimal combination of resolution and sensitivity for organ-specific imaging of small animals, and the single-pinhole collimator enables high-resolution whole-body imaging of small animals.

Keywords: Molecular Imaging; Nuclear Medicine; SPECT; Animal Imaging Instrumentation; Monte Carlo Method; Computer-Assisted Image Processing; Imaging Phantoms

1 Introduction

Functional imaging in nuclear medicine extensively employs positron emission tomography (PET) and single-photon emission computed tomography (SPECT) for disease diagnosis and staging, therapy planning, dosimetry, and monitoring of treatment response [1]. These nuclear medicine techniques are based on radiopharmaceutical uptake within the body, yielding critical diagnostic information that can readily translate to developing theranostic strategies for managing various diseases. Such investigations are now commonly performed in the preclinical setting to evaluate the effects of novel drugs and therapies in small animals [2]. Due to the relatively small organ size of mice compared to humans, preclinical imaging demands high-resolution technology. Recent advancements in imaging technology have promoted widespread adoption of small-animal imaging, and the availability of dedicated preclinical scanners has increased to satisfy this demand. Some advantages of SPECT over PET include superior spatial resolution, simultaneous multi-energy and multi-isotope signature detection, increased accessibility to isotopes with a range of physical half-lives, relatively simple and stable radiochemistry with increased specific activities, and reduced production costs [3, 4]. Therefore, developing sensitive and accurate preclinical SPECT systems is of growing importance.

Monte Carlo simulations are also essential in emission tomography investigations to model, develop, and evaluate nuclear-based imaging systems [5]. The Monte Carlo method is considered the gold standard for designing new medical imaging devices, offering an effective means to assess performance, optimize acquisition protocols, and evaluate new image reconstruction algorithms and correction techniques. Several Monte Carlo packages exist including Geometry and Tracking (Geant4) [6], Electron Gamma Shower (EGS) [7], and Monte Carlo N-Particle (MCNP) [8], all of which provide well-validated physics models and geometry modelling tools. These toolkits focus on radiation transport simulations, and tuning the code to model

PET and SPECT devices can be challenging. The Geant4 Application for Tomographic Emission (GATE) aims to simplify the modelling process while accommodating complex scanner geometries and imaging configurations using geometric definitions, time-dependent phenomena, radioactive source definitions, detector electronics modelling, and data output [5].

Several commercially available preclinical SPECT detectors have been investigated with GATE, including X-SPECT (TriFoil Imaging, Chatsworth, USA) [9], Inveon (Siemens, Munich, Germany) [10], HiReSPECT (Parto Negar Persia, Tehran, Iran) [11], and NanoSPECT/CT$^{\text{PLUS}}$ (Mediso, Budapest, Hungary) [12] scanners. These systems, like all SPECT systems, are constructed with varying component designs, including but not limited to pinhole or parallel-hole collimators, monolithic or pixelated scintillators, and solid-state or vacuum tube detector technologies. Cameras that use photomultiplier tubes (PMTs) for high-resolution preclinical SPECT are large and bulky and require highly magnifying pinhole collimators to overcome the limiting intrinsic spatial resolution of PMTs. While position-sensitive PMTs (PSPMTs) offer a smaller form factor than PMTs with improved resolution, their combination with scintillating crystals to detect γ- and X-rays yields a detector that is also several centimeters thick, and the camera size is further increased when attaching pinhole or parallel-hole collimators. Recent advancements in solid-state technology, such as cadmium zinc telluride (CZT) for direct detection or silicon-photomultipliers (SiPMs) coupled with scintillators for indirect detection, provide advantages over PMT-based technology, including a smaller form factor for design flexibility, superior intrinsic spatial resolution, reduced power consumption, and insensitivity to magnetic fields and vibrations [13]. An example of a novel SiPM-based preclinical SPECT scanner is the Cubresa Spark (Cubresa Inc., Winnipeg, Canada).

The Spark is a small-animal benchtop SPECT system optimized for *in vivo* mouse imaging and can be configured with up to two detector heads. Its current configu-

ration features one detector head, single- and multi-pinhole collimators, a sodium-activated cesium iodide (CsI(Na)) scintillator, and a SiPM array to achieve high-resolution planar and tomographic imaging. Altogether, the detector head is less than 6 cm-thick from the face of the collimator to the exterior of the back compartment housing the electronics. This small form factor makes the Spark suitable for benchtop use. It can also be attached to preclinical computed tomography (CT) scanners for multi-modal disease study, translational research, and drug discovery applications. For example, it was recently utilized in developing diagnostic radiopharmaceuticals for Alzheimer's disease [14]. Due to the novelty of SiPMs in SPECT, the performance characteristics of a preclinical SiPM SPECT scanner have not been established or compared to other scanners in the literature.

To compare different γ-cameras, the National Electrical Manufacturers Association (NEMA) has published the NEMA NU 1-2018 Standard for Performance Measurements of Gamma Cameras [15]. This standard provides a uniform and consistent method for measuring and reporting performance parameters for various camera designs. Although NEMA has published a *clinical* and *preclinical* standard for PET scanners, a preclinical SPECT standard is currently unavailable. However, the NEMA NU 1-2018 clinical standard can be readily applied or extended to preclinical SPECT cameras with minor modifications. NEMA standards also provide a rigorous and thorough approach to validating Monte Carlo models, unlike the systems above modelled in GATE that used widely varying, incomplete, or untraceable validation approaches in some cases.

The primary objective of this study is to evaluate the performance characteristics of a high-resolution SiPM-based preclinical SPECT scanner — the Cubresa Spark — according to the NEMA NU 1 Standard for Performance Measurements of Gamma Cameras. A secondary objective is to configure and validate a GATE simulation model of the Spark using the measured NEMA results. Collectively, this study aims

82 to accurately establish the imaging performance of a SiPM SPECT system in planar

83 and tomographic acquisitions offering critical insight into its utility in supporting

84 the development of novel molecular imaging agents and techniques.

85 Methods and materials

86 *Equipment description*

87 The Spark (Fig. 1) was affixed to the benchtop of a Triumph LabPET4/CT dual-

88 modality system (TriFoil Imaging, Chatsworth, USA). Its detector housing was

89 manufactured from tungsten and assembled with a $102{\times}102{\times}3$ mm^3 monolithic

90 CsI(Na) scintillator (Saint-Gobain Crystals, Hiram, USA) and a $14{\times}14$ SensL C-

91 series SiPM array with 6 mm sensors (ON Semiconductor, Phoenix, USA). As out-

92 lined in Table 1, the Spark performance was assessed with two interchangeable

93 tungsten collimators (Scivis GmbH, Göttingen, Germany): a single-pinhole (SPH)

94 collimator for high-resolution planar and tomographic imaging, and a multiplexing

95 multi-pinhole (MPH) collimator for high-resolution tomography with increased sen-

96 sitivity. The SPH collimator has a non-focusing right-circular double-cone pinhole,

97 and the MPH collimator uses a $5{\times}5$ array of focusing right-circular double-cone

98 pinholes where each row focuses on a different volume of interest (VOI) in the to-

99 mographic field of view (FOV) [16]. The area of the detector used for imaging γ-

100 and X-rays has a useful field of view (UFOV) and central field of view (CFOV) of

101 84.5 mm and 63.375 mm, respectively, as defined by the collar of the collimators.

102 → **Figure 1 goes here.**

Table 1 Geometric specifications of pinhole collimators.

Aperture[1]	SPH	MPH
Pinhole diameter (mm)	1.0	1.0
Pinhole acceptance angle (°)	90.0	25.0
Number of pinholes	1	25
Thickness (mm)	10.0	10.0
Radius of rotation (mm)	28.0	28.0
Aperture-to-detector distance[2] (mm)	26.75	26.75
Reconstructed axial FOV (mm)	57.0	14.0
Reconstructed transaxial FOV (mm)	46.0	30.0

[1]SPH: Single-pinhole, MPH: Multi-pinhole
[2]Measured to face of scintillator

The Spark was delivered with Scivis' HiSPECT reconstruction software, which was preconfigured solely for the MPH collimator. Precise information regarding the MPH collimator geometry was not readily available, and as a result, this restricted the simulation model to the SPH collimator only. Measured and simulated SPH SPECT images were reconstructed with prototype code developed for the open-source Software for Tomographic Image Reconstruction (STIR) [17, 18, 19]. This reconstruction code is currently under development and will be the focus of future work; however, details will be provided as necessary when used in this work.

Prior to measurement, the SPECT system was calibrated for energy, linearity, uniformity, center of rotation, and aperture-to-detector distance [20, 21]. Radionuclide activity measurements were performed with a Capintec CRC-55tR dose calibrator (Mirion Technologies, Florham Park, USA). Various phantoms and source positioning jigs were fabricated in-house to adhere to the NEMA protocol, and each required device is described in the following sections.

Simulation description

A model of the Spark detector head (Fig. 1) was created using the SPECThead system in the GATE v9.0 Monte Carlo toolkit [5] compiled with Geant4 10.06.p01 [6] and Rapid Object-Oriented Technology (ROOT) 6.14.04 [22]. Simulations were distributed over 12 cores on an HP Z820 workstation operating Ubuntu 18.04.5 LTS with two Intel Xeon E5-2630 2.3 GHz hexa-core CPUs and 64 GB of 1600 MHz DDR3 memory. ROOT output was combined into one file and then converted to Cubresa's list mode format for further processing.

Complex detector geometry was modelled with standard tessellation language (STL) files provided by Cubresa, and simple geometric volumes were modelled with predefined shapes available in GATE. Note that the animal bed and MPH collimator were excluded from simulation. The SPH collimator was modelled with a 0.85 mm diameter pinhole to better match the simulated collimator-detector response func-

130 tion to measurement. Physics processes were initialized with the Geant4 standard

131 electromagnetic physics package option 4 (emstandard_opt4) [6]. Particle produc-

132 tion cuts were set at the default value of 1 mm corresponding to a few keV in most

133 materials, except the scintillator and pinhole knife-edge where the threshold was set

134 to 1 keV. Radioactive sources were defined as an isotropic UserSpectrum source of

135 γ-rays with isotope spectra defined from the Table of Radionuclides [23]. The scin-

136 tillation process, optical photon transport, and light detection were not simulated

137 to save computing time.

138 The signal processing chain of the simulation was modelled using the following

139 digitizer modules: the adder, readout, energy blurring, spatial blurring, pile-up, dead

140 time, and efficiency. Figure 2 presents the digitizer chain with the values set for

141 parameters of interest. All simulation parameters were deduced from measurement

142 except for the pile-up timing resolution $t_{\min}$, which was calculated as

$$t_{\min} = \frac{P_1}{R_{\mathrm{T}}(P_0 + 2P_1)} \tag{1}$$

144 where P_0 and P_1 are the counts in the primary and first order pile-up peaks, re-

145 spectively, and R_{T} is the true input count rate [24].

146 → **Figure 2 goes here.**

147 NEMA performance characterization and SPECT model validation

148 Performance characterization of the Spark was made according to the NEMA NU

149 1-2018 protocol, with tests briefly described in the following sections. The radionu-

150 clide for all tests was technetium-99m (^{99m}Tc) unless stated otherwise. Projection

151 images of the UFOV and CFOV were generated with electronic masking using 30%-

152 wide energy windows centered on the reference photopeak(s), and 0.1 mm isotropic

153 pixels were used unless stated otherwise. Measured data were acquired according to

154 total acquisition time or counts through an open energy window. Simulations were

155 then configured based on measurements of data acquisition time, radioactivity, ra-

156 dioactive source distribution, and system geometry, except for the SPH collimator

157 pinhole diameter. No corrections were applied to the simulated data at any stage.

158 Validation of the GATE model was based on reporting parameter comparisons be-

159 tween measured and simulated NEMA results.

Tests of intrinsic gamma camera detector characteristics

161 *Intrinsic spatial resolution and linearity*

162 Intrinsic spatial resolution refers to the γ-camera's ability to localize an ionizing

163 photon's interaction site within the detector, and intrinsic linearity reflects the dis-

164 tortion of those interaction sites throughout the detector's FOV. This test was

165 performed with a 2.5 mm-thick tungsten planar mask comprised of a 3×3 grid of

166 0.8 mm-wide and 26.5 mm-long parallel slits having adjacent slit centers separated

167 by 31.5 mm, and a Derenzo pattern with {0.7, 0.8, 0.9, 1.0, 1.2, and 1.4} mm di-

168 ameter holes. An Eppendorf tube containing a 50 MBq point source was centered

169 65 cm above the face of the detector, and 15 million counts were acquired. Intrinsic

170 resolution and linearity were assessed from line spread functions (LSFs) and an-

171 alyzed according to the procedures defined by the NEMA NU 1-2018 protocol. A

172 millimeters-per-pixel calibration factor was also calculated using line profile spacing

173 to convert relevant image dimensions to physical units in relevant NEMA tests.

174 Note that the mask-slit geometry above did not yield the limiting spatial resolu-

175 tion. Therefore, a secondary test was performed with a pencil beam to measure the

176 limiting resolution from a point spread function (PSF). A pencil beam was created

177 with a tungsten line-source holder with a tunnel 0.4 mm in diameter ($\varnothing$), 10.0 mm

178 in length (L), and centered 1.0 mm above the detector with a 1.0 cm-thick alu-

179 minium plate. A total of 100,000 counts were acquired from a 170 MBq line source

180 established in a capillary tube ($\varnothing_{inner} = 1.15$ mm, $\varnothing_{outer} = 1.50$ mm, $L = 75$ mm).

Intrinsic flood field uniformity

The intrinsic uniformity quantifies the γ-camera's response to a uniform radiation flux. An 8 MBq point source was centered 65 cm above the face of the detector and 100 million counts were acquired. The measured and simulated flood field projection images with 1 mm pixels were smoothed once by convolution with the NEMA smoothing filter, and measured data were corrected for uniformity. The integral uniformity was calculated using

$$\text{Uniformity } (\%) = \frac{\max - \min}{\max + \min} \times 100 \tag{2}$$

where max and min refer to the maximum and minimum pixel values within the FOV. Similarly, the differential uniformity was calculated with Eq. 2 from the max and min in a set of five contiguous pixels in a row or column.

Multiple window spatial registration

The multiple window spatial registration (MWSR) test was performed with 11 MBq of ^{67}Ga to assess the Spark's ability to accurately localize photons of different energies when imaged through different energy windows. The previously described pencil beam source holder (see Intrinsic spatial resolution and linearity) was positioned in a 1.0 cm-thick aluminium plate at nine locations along the detector axes, including the center of the detector, 0.4×, and 0.8× the distance to the edge of the UFOV. A total of 4 million counts were acquired at each position, and projection images were generated from each photopeak. The maximum axial and transaxial displacements of PSF centroids were then calculated. Overall spatial registration accuracy was also assessed according to the mean Euclidean distance between each centroid and the average centroid location.

Intrinsic count rate performance in air: Decaying source method

The count rate performance describes the γ-camera's ability to process one detec-

206 tion event before moving on to another. However, the number of recorded counts

207 may be fewer than true events because of dead time and/or pile-up. Two models

208 exist to describe idealized dead time behaviour: paralyzable and non-paralyzable

209 dead time [25]. The Spark's behaviour is well-described with a paralyzable model

210 following the equation

211
$$\text{OCR} = \text{ICR } e^{-\text{OCR}\tau} \tag{3}$$

212 where OCR is the observed count rate, ICR is the input count rate, and τ is the

213 system dead time. Furthermore, OCR can be affected by pile-up, which occurs when

214 a true event at time $t = 0$ is followed by subsequent events in the interval $0 < t < \tau$,

215 followed by an event-free interval of length τ. Using the decaying source method,

216 the dead time was calculated from the intercept and slope of Eq. 4:

217
$$\lambda t + \ln \text{OCR} = -\text{ICR}_0 \tau e^{-\lambda t} + \ln \text{ICR}_0 \tag{4}$$

218 where λ is the decay constant, t is the time, ICR_0 is the true input rate at the

219 beginning of measurement, $e^{-\lambda t}$ is the abscissa, and $\lambda t + \ln \text{OCR}$ is the ordinate [25].

220 Care was taken to minimize scatter during count rate performance assessment by

221 securing an Eppendorf tube containing 235 MBq in a tungsten Capintec 511 Dose

222 Drawing Syringe Shield. The shield was capped with a lead lid, and a 6.0 mm-thick

223 copper plate covered the open side of the source holder. The source was placed at a

224 distance of 5×UFOV above the detector face to produce a uniform radiation field.

225 Counts were measured for 60 s and simulated for 10 s in 60 min intervals, and the

226 last data point was acquired when the observed count rate dropped below 600 cps

227 to determine ICR_0 accurately. All data were corrected for radioactive decay, and the

228 measured data were corrected for background noise and uniformity. Measured count

229 rate data were utilized to configure the digitizer's pile-up, dead time, and efficiency

230 modules. Following the NEMA protocol, the intrinsic count rate performance was

231 analyzed in terms of the maximum OCR and 20% loss OCR.

232 *Intrinsic energy resolution*

233 The energy resolution characterizes a radiation detector's response to a monoen-

234 ergetic radiation source and describes its ability to distinguish between different

235 energies of that radiation. The formal definition is

$$236 \quad \text{Energy resolution (\%)} = \frac{\text{FWHM}}{\text{Photopeak location}} \times 100 \quad (5)$$

237 where FWHM is the full width at half maximum of the photopeak calculated ac-

238 cording to NEMA's resolution methodology in this context. The Spark's intrinsic

239 energy resolution was assessed using 0.6 keV bins with the count rate data point

240 immediately below the 20% loss OCR introduced in the previous section (Intrinsic

241 count rate performance in air: Decaying source method). This data point satis-

242 fies all NEMA conditions while offering count rate traceability. The simulated data

243 point below the 20% loss OCR was re-simulated with a 60 s acquisition time to ob-

244 tain count statistics comparable to the measurement. Note that a keV-per-channel

245 calibration factor was not calculated with cobalt-57 (^{57}Co) since a vendor-specific

246 energy calibration is automatically applied to list mode data.

247 **Tests of gamma camera detectors with collimators**

248 In this study, system or *extrinsic* measurements primarily involved the SPH collima-

249 tor due to its applicability in planar scintigraphy yielding unambiguous projection

250 images. Measurements with the experimental MPH were included where applicable.

251 *System spatial resolution without scatter*

252 The system spatial resolution without scatter represents the γ-camera's limit-

253 ing ability to localize a photon interaction site in the detector when combin-

254 ing collimator and intrinsic factors. Acquisitions were performed in the axial

255 and transaxial directions using a precision capillary tube ($\varnothing_{\mathrm{inner}} = 0.4$ mm,

256 $\varnothing_{\mathrm{outer}} = 0.8$ mm, $L = 75$ mm). The capillary tube contained 10 MBq of radioac-

257 tivity, and 100,000 counts were acquired at positions of {0.4, 25.0, 50.0, 75.0, and

258 100.0} mm from the face of the SPH collimator. NEMA's resolution methodology

259 was applied to calculate resolution from LSFs. Results were corrected for magni-

260 fication to compare resolution in the object rather than the detector. A plot of

261 the average system resolution as a function of source-to-collimator distance was

262 generated with a linear least squares fit to characterize the system resolution.

System spatial resolution with scatter

264 The presence of a scattering medium degrades image quality in terms of projection

265 image blurring, reduced contrast in reconstructed images, and decreased quantita-

266 tive accuracy [26]. Thus, the system spatial resolution with scatter was assessed

267 with a custom mouse phantom inspired by the NEMA NU 1-2018 standard and the

268 micro-PET scatter phantom defined in the NEMA NU 4-2008 standard for preclin-

269 ical PET [27]. The custom mouse phantom was fabricated from an acrylic cylinder

270 ($\varnothing = 25.4$ mm, $L = 60$ mm) with three 0.8 mm-diameter bores for precision capil-

271 lary tubes: one at the center and two separated by 90° with a 10 mm radial offset.

272 One precision capillary tube containing 10 MBq was inserted into the central bore

273 of the custom phantom, and 100,000 counts were acquired axially and transaxially

274 at capillary tube positions of {12.7, 25.0, 50.0, 75.0, and 100.0} mm from the face

275 of the collimator. Analysis of the resulting projection images was identical to the

276 methods outlined in System spatial resolution without scatter.

System planar sensitivity

278 The system planar sensitivity characterizes the number of detected counts per unit

279 activity to evaluate a collimator's count rate performance. A petri dish with a

280 35.0 mm diameter was filled with 2 ml of water and injected with a calibrated activ-

281 ity of $A_{\text{cal}} = 210$ MBq for the SPH dataset and $A_{\text{cal}} = 25$ MBq for the MPH dataset.

282 The internal base of the radioactive solution was placed at source-to-collimator dis-

283 tances of $D = \{10.0, 20.0, 28.0, 50.0, \text{ and } 100.0\}$ mm, and 4 million counts were

284 collected at each position in measurement. In contrast, counts were collected for

285 100 s at each position in simulation to save on computing time. Data were acquired

286 from the largest to the smallest distance with activity levels ranging from A_{cal} to

287 ~ 15 MBq to minimize pile-up and dead time effects, namely in the SPH acquisition.

288 Measured data were corrected for uniformity, and then the decay-corrected count

289 rate R was calculated for each acquisition i as

$$R_i = \lambda C_i \mathrm{e}^{\lambda(T_i - T_{\text{cal}})} \times \left(1 - \mathrm{e}^{-\lambda T_{\text{acq},i}}\right)^{-1} \tag{6}$$

291 where C_i is the summed counts from the projection image, T_i is the acquisition start

292 time, $T_{\text{acq},i}$ is the acquisition duration, and T_{cal} is the time of activity calibration.

293 Using a standard Levenberg-Marquardt non-linear least squares fit technique, the

294 decay-corrected count rate and source-to-collimator distance for each SPH acquisi-

295 tion were fit with the function

$$R_i = c_0 + c_1 \mathrm{e}^{(-c_2 D_i)} \tag{7}$$

297 where c_0, c_1, and c_2 are fitting parameters. The total system sensitivity S_{TOT} was

298 then calculated as

$$S_{\text{TOT},i} = \frac{R_i}{A_{\text{cal}}} \tag{8}$$

300 and plotted against the source-to-collimator distance to characterize the sensitivity.

301 Note that NEMA's protocol utilizes fit parameters from Eq. 7 to compute a collima-

302 tor penetration factor for counts in a given region of interest (ROI). This analysis

303 was excluded as it does not apply to pinhole collimators. Furthermore, Eq. 7 does

304 not apply to the MPH collimator due to the focusing orientation of pinholes.

Tests specific to tomographic camera systems

306 SPECT projection data were acquired from 0° to 270° in a 208×208 matrix with

307 0.5 mm isotropic pixels, then reconstructed with nine iterations of the maximum

308 likelihood expectation maximization (MLEM) algorithm in 0.25 mm isotropic vox-

309 els. SPH SPECT data were acquired in 3° increments then reconstructed with STIR

310 in a 230×184×184 matrix, and MPH SPECT data were acquired in 90° increments

311 then reconstructed with HiSPECT in an 80×144×144 matrix. HiSPECT software

312 only supports the MLEM algorithm, whereas STIR's pinhole-SPECT software per-

313 mits access to STIR's extensive library of algorithms and corrections for the spatially

314 variant collimator-detector response and attenuation. Thus, SPH SPECT data were

315 also reconstructed with the filtered back projection (FBP) algorithm using a ramp

316 filter to adhere to the NEMA protocol.

SPECT reconstructed spatial resolution without scatter

318 The reconstructed spatial resolution without scatter reflects the limiting size of

319 a radioactive distribution that can be observed with the γ-camera. Three point

320 sources in air were established in precision capillary tubes with a mean activity of

321 0.274 ± 0.007 MBq and an axial extent of $\sim$0.4 mm. To conform to the small recon-

322 structed FOV of the MPH collimator (see Table 1), one point source was centered on

323 the axis of rotation, and the two remaining point sources were positioned at $\pm 75\%$

324 of the distance to the edge of the FOV, i.e., ± 5.25 mm axially and ± 11.25 mm

325 transaxially. The point sources were set in place, and 300,000 counts were acquired

326 across all projections in the SPH and MPH acquisitions to directly compare to-

327 mographic resolution. Cubic ROIs were centered around each reconstructed point

328 source and summed along each axis to calculate the radial, tangential, and axial

329 resolution without scatter according to the NEMA protocol.

SPECT reconstructed spatial resolution with scatter

331 The reconstructed spatial resolution with scatter was assessed with the custom

332 mouse phantom described in System spatial resolution with scatter. Three capillary

333 tubes containing a mean activity of 9.4 ± 0.1 MBq were inserted into the phantom

334 and centered axially in the FOV with peripheral line sources placed at $0°$ and

335 $270°$ to maximize the amount of scatter contributing to projection images over the

336 extent of rotation. The line sources in the custom mouse phantom were set in place,

337 and 5 million counts were acquired across all projections in the SPH and MPH

338 acquisitions to directly compare tomographic resolution. The reconstructed images

339 were summed axially to obtain three 3.5 mm-thick transverse slices: one at the

340 center of the FOV and two at $\pm 75\%$ the distance to the edge of the respective axial

341 FOV. A square ROI was centered on each resulting PSF to calculate the central,

342 radial, and tangential resolution with scatter according to the NEMA protocol.

SPECT volume sensitivity and uniformity

344 The system volume sensitivity (SVS) reports the total system sensitivity to a

345 uniform activity concentration in a cylindrical phantom. An acrylic phantom

346 ($\varnothing_{\text{inner}} = 26$ mm, $\varnothing_{\text{outer}} = 28$ mm, $L_{\text{inner}} = 21$ mm) was filled with water con-

347 taining 1.75 MBq/ml then centered along the axis of rotation in the γ-camera's

348 image space. The phantom was set in place, and SPH and MPH SPECT acquisi-

349 tions were obtained with 10 s and 60 s projections, respectively. The measured data

350 were corrected for uniformity, and then the SVS was calculated as

$$\text{SVS} = \frac{A}{B_{\text{c}}} \tag{9}$$

352 where A is the average count rate (total counts divided by total elapsed time in-

353 cluding time for rotation) and B_{c} is the activity concentration halfway through the

354 acquisition. By normalizing the SVS by the axial extent L of the cylindrical phan-

355 tom in the reconstructed image, the volume sensitivity per axial centimeter (VSAC)

356 was calculated as

$$\text{VSAC} = \frac{\text{SVS}}{L}. \tag{10}$$

358 The VSAC was then multiplied by the reconstructed axial FOV of the collimator to

359 obtain a useful approximation of the total system response to a broad distribution

360 of radioactivity.

361   Although it is not a defined NEMA test, the volume uniformity was evaluated

362 from images of the cylindrical phantom reconstructed with the MLEM algorithm.

363 Integral uniformity was calculated with Eq. 2 from a VOI covering 75% of the

364 phantom's imaged length and 60% of the phantom's inner diameter. Within this

365 VOI, the root-mean-square (RMS) noise was also calculated as

$$\text{RMS noise } (\%) = \frac{\sigma}{\mu} \times 100 \tag{11}$$

367 where σ is the standard deviation and μ is the mean voxel value within the VOI [28].

368 Results

369 *Tests of intrinsic gamma camera detector characteristics*

370 Intrinsic spatial resolution and linearity

371 Representative planar mask projection images from measured and simulated ac-

372 quisitions are presented in Fig. 3, and Table 2 gives the intrinsic spatial resolution

373 determined from the pencil beam PSF and planar mask LSFs in terms of the FWHM

374 and full width at tenth maximum (FWTM). The pencil beam produced a measured

375 and simulated limiting intrinsic spatial resolution of 0.85 mm, which was ~7% below

376 that predicted by the planar mask slits. Table 2 also presents the differential and

377 absolute intrinsic spatial linearity results, which were found to be $\lesssim$ 0.1 mm in mea-

378 surement and simulation. The measured and simulated linearity results calculated a

379 calibration factor of 0.099 mm/pixel. Altogether, good agreement was observed be-

380 tween measurement and simulation, and measured results indicated highly accurate

381 positioning and minimal distortion of detected photons with the SiPM array.

382 → **Figure 3 goes here.**

Table 2 Intrinsic spatial resolution and linearity.

Reporting parameter	Region of interest	Measurement	Simulation
Resolution PSF FWHM (mm)	Center of FOV	0.851 ± 0.010	0.850 ± 0.003
Resolution PSF FWTM (mm)	Center of FOV	1.559 ± 0.014	1.591 ± 0.007
Resolution LSF FWHM (mm)	UFOV	0.912 ± 0.098	0.916 ± 0.026
	CFOV	0.953 ± 0.091	0.924 ± 0.029
Resolution LSF FWTM (mm)	UFOV	1.73 ± 0.15	1.66 ± 0.03
	CFOV	1.80 ± 0.14	1.68 ± 0.03
Differential linearity (mm)	UFOV	0.023	0.001
	CFOV	0.024	0.002
Absolute linearity (mm)	UFOV	0.102	0.003
	CFOV	0.055	0.003

383 *Intrinsic flood field uniformity*

384 Integral and differential uniformity calculated from the UFOV and CFOV of flood

385 field images are presented in Table 3. The measured and simulated uniformity results

386 were < 3% and < 2%, respectively, showing good agreement and uniform response

387 to radiation.

Table 3 Flood field uniformity.

Reporting parameter	Region of interest	Measurement	Simulation
Integral uniformity (%)	UFOV	2.96	1.72
	CFOV	2.79	1.96
Row differential uniformity (%)	UFOV	2.75	1.69
	CFOV	2.52	1.77
Column differential uniformity (%)	UFOV	2.75	1.67
	CFOV	2.11	1.67

388 *Multiple window spatial registration*

389 The higher energy γ-rays from ^{67}Ga were observed to penetrate the walls of the

390 tungsten pencil beam holder and produce noisy projection images, resulting in a

391 significant fraction of total counts detected outside the pencil beam PSF. Nonethe-

392 less, the measured (simulated) MWSR was found to have maximum PSF centroid

393 displacements in the axial and transaxial directions of 0.192 mm (0.095 mm) and

394 0.259 mm (0.149 mm), respectively, which reflects the worst-case-scenarios of mis-

³⁹⁵ registration. The mean Euclidean distance between each centroid and the aver-

³⁹⁶ age centroid location for a given pencil beam location was 0.050 ± 0.023 mm and

³⁹⁷ 0.044 ± 0.022 mm in measurement and simulation, respectively. In other words,

³⁹⁸ photons of different energies were accurately localized, and centroids from different

³⁹⁹ energy windows were found within one pixel of each other on average.

⁴⁰⁰ *Intrinsic count rate performance in air: Decaying source method*

⁴⁰¹ Figure 4 presents the ^{99m}Tc count rate performance curve where the measured

⁴⁰² (simulated) maximum and 20% loss OCRs were 15,410 cps (15,500 cps) and

⁴⁰³ 7,520 (7,440 cps), respectively. The measured data were corrected for uniformity

⁴⁰⁴ and a background count rate of 11.6 cps to directly compare with the simulation

⁴⁰⁵ for which no corrections were necessary. The measured and simulated results were

⁴⁰⁶ comparable at input count rates below the maximum. However, the experimental

⁴⁰⁷ detector did not behave like an idealized paralyzable system at relatively large count

⁴⁰⁸ rates. Unexpected behaviour was observed through photopeak shifting in addition

⁴⁰⁹ to pulse pile-up and dead time effects at count rates beyond the maximum — a

⁴¹⁰ count rate range unlikely to be encountered with typical *in vivo* usage of the Spark.

⁴¹¹ The measured (simulated) dead time was found to be 23.9 μs (23.8 μs) using Eq. 4.

⁴¹² → **Figure 4 goes here.**

⁴¹³ *Intrinsic energy resolution*

⁴¹⁴ Energy spectra are presented in Fig. 5 where the intrinsic energy resolution was

⁴¹⁵ 14.7% in measurement and simulation. Minute differences can be observed in the

⁴¹⁶ energy spectra at energies above the photopeak due to incomplete scintillation light

⁴¹⁷ collection during pile-up in the experimental system. Aside from the differences in

⁴¹⁸ pile-up energy distribution, a 3.1% difference was found in the number of pile-up

⁴¹⁹ events detected in an energy window extending above 150 keV.

⁴²⁰ → **Figure 5 goes here.**

Tests of gamma camera detectors with collimators

System spatial resolution without scatter

The system spatial resolution without scatter is shown in Fig. 6. A linear least squares fit to the measured and simulated data calculated a coefficient of determination of $r^2 = 1.0$ and similar FWHM line equations. The FWHM equations predicted a measured (simulated) limiting system spatial resolution of 1.87 mm (1.80 mm) at the center of rotation ($D = 23.0$ mm). Overall, the FWHM differences between measurement and simulation varied from 4.8% to 3.2% over source-to-collimator distances from 0 mm to 100 mm, respectively. A discrepancy can be observed in the FWTM best-fit lines.

$\rightarrow$ **Figure 6 goes here.**

System spatial resolution with scatter

The system spatial resolution with scatter in the custom mouse phantom is presented in Fig. 7. Linear least squares fits calculated a coefficient of determination of $r^2 = 1.0$ and comparable FWHM and FWTM fit equations between measurement and simulation. The FWHM equations predicted a measured (simulated) system spatial resolution with scatter of 1.98 mm (1.88 mm) at the center of rotation. Here, the FWHM differences between measurement and simulation varied from 7.1% to 2.9% over source-to-collimator distances from 0 mm to 100 mm, respectively. Interestingly, the FWTM best-fit lines have a higher degree of correspondence between measurement and simulation with scatter than without.

$\rightarrow$ **Figure 7 goes here.**

System planar sensitivity

The total system planar sensitivity is presented in Fig. 8 for the SPH and MPH collimators. For the SPH collimator, the exponential fit calculated a measured (simulated) planar sensitivity of 33.8 cps/MBq (35.2 cps/MBq) at the center of rotation, reflecting a 4.0% difference. The difference increased to 14.2% at the face of the col-

448 limator, which could be partly due to limitations in modelling the collimator with

449 a 0.85 mm pinhole. For the MPH collimator, sensitivity is optimized within the

450 tomographic FOV due to the focusing nature of the pinholes. Therefore, the three

451 largest values were fit with a quadratic function, and interpolation at the center of

452 rotation calculated a planar sensitivity of 150 cps/MBq.

453 → **Figure 8 goes here.**

454 ***Tests specific to tomographic camera systems***

455 *SPECT reconstructed spatial resolution without scatter*

456 Table 4 details the three-dimensional (3D) resolution results from all reconstructed

457 point source images. Acquisitions with the SPH collimator calculated a measured

458 (simulated) limiting 3D resolution of 1.37 ± 0.15 mm (1.30 ± 0.15 mm). The MPH

459 collimator yielded a 13% improvement in the limiting 3D resolution with a value

460 of 1.19 ± 0.20 mm and a submillimeter tangential resolution (0.91 ± 0.05 mm)

461 due to the lateral focusing pinholes. Note that leaching of radioactivity into the

462 capillary tube sealing clay was observed in measured tomographic images. A closer

463 inspection of Table 4 confirms that the axial resolutions were overestimated in

464 measurement when considering that all other FWHM were nearly identical between

465 SPH collimator measurement and simulation.

Table 4 SPECT reconstructed spatial resolution without scatter.

Reporting parameter	Measurement			Simulation	
Collimator	MPH	SPH	SPH	SPH	SPH
Reconstruction algorithm	MLEM	MLEM	FBP	MLEM	FBP
Central transaxial FWHM (x,y) (mm)	1.29 ± 0.04	1.45 ± 0.01	2.26 ± 0.01	1.50 ± 0.01	2.26 ± 0.01
Central axial FWHM (z) (mm)	1.56 ± 0.01	1.58 ± 0.01	2.45 ± 0.01	1.31 ± 0.01	2.26 ± 0.01
Peripheral radial FWHM (x) (mm)	1.13 ± 0.08	1.25 ± 0.06	2.03 ± 0.10	1.30 ± 0.09	2.11 ± 0.25
Peripheral tangential FWHM (y) (mm)	0.91 ± 0.05	1.23 ± 0.11	1.94 ± 0.14	1.26 ± 0.13	1.93 ± 0.10
Peripheral axial FWHM (z) (mm)	1.24 ± 0.04	1.45 ± 0.16	2.70 ± 0.04	1.12 ± 0.06	2.48 ± 0.05
Average 3D FWHM (mm)	1.19 ± 0.20	1.37 ± 0.15	2.26 ± 0.30	1.30 ± 0.15	2.20 ± 0.23

SPECT reconstructed spatial resolution with scatter

Figure 9 presents the central 3.5 mm-thick slice of the custom mouse phantom from the MLEM reconstructions, and Table 5 gives a breakdown of the in-plane resolution values from all reconstructed mouse phantom images. Acquisitions with the SPH collimator produced a measured (simulated) average in-plane resolution of 1.44 ± 0.07 mm (1.46 ± 0.07 mm), and the MPH collimator yielded a 17% improvement with an average FWHM of 1.18 ± 0.15 mm. Measurement and simulation were found to have an excellent agreement in tomographic resolution with differences below 2%. Although the MPH collimator is capable of higher resolution than the SPH collimator, the reduced standard deviation of the SPH resolution indicates that its in-plane resolution is more symmetric throughout the tomographic FOV.

→ **Figure 9 goes here.**

Table 5 SPECT reconstructed spatial resolution with scatter.

Reporting parameter	Measurement			Simulation	
Collimator	MPH	SPH	SPH	SPH	SPH
Reconstruction algorithm	MLEM	MLEM	FBP	MLEM	FBP
Central FWHM (mm)	1.29 ± 0.05	1.52 ± 0.04	2.23 ± 0.07	1.54 ± 0.05	2.21 ± 0.08
Radial FWHM (mm)	1.27 ± 0.06	1.39 ± 0.06	2.34 ± 0.11	1.40 ± 0.04	2.30 ± 0.06
Tangential FWHM (mm)	0.99 ± 0.07	1.41 ± 0.03	2.03 ± 0.11	1.43 ± 0.03	2.06 ± 0.10
Average in-plane FWHM (mm)	1.18 ± 0.15	1.44 ± 0.07	2.20 ± 0.16	1.46 ± 0.07	2.19 ± 0.12

SPECT volume sensitivity and uniformity

Tomographic images of the cylindrical phantom reconstructed with the MLEM algorithm are presented in Fig. 10, and the corresponding volume sensitivity, uniformity, and RMS noise results are given in Table 6. When comparing the measurement to simulation, the SPH volume sensitivity had the largest discrepancy observed across all NEMA tests, with a difference of 7.3%. This can be attributed to the slight overestimation in simulated sensitivity and an air bubble in the phantom during measurement that increased the source-to-collimator distance on average. Although the SPH collimator has fewer pinholes than the MPH collimator and uti-

lizes a smaller area of the UFOV, its increased tomographic FOV and total system response compensate for the relatively low sensitivity. Furthermore, tomographic images produced with the SPH collimator are significantly more uniform and less noisy than those made with the MPH collimator.

→ **Figure 10 goes here.**

Table 6 SPECT volume sensitivity and uniformity.

Reporting parameter	Measurement		Simulation
Collimator	MPH	SPH	SPH
SVS (cps/(MBq/cm^3))	2,200	329	354
VSAC (cps/(MBq/cm^2))	1,570	157	169
Total system response (cps/(MBq/cm^3))	2,200	901	970
Integral uniformity (%)	96.5	48.2	38.2
RMS noise (%)	38.7	11.6	10.2

Discussion

The performance characteristics of a high-resolution SiPM-based preclinical SPECT system — the Cubresa Spark — have been evaluated for the first time according to the NEMA NU 1-2018 Standard for Performance Measurements of Gamma Cameras. The primary challenge in applying the NEMA NU 1 standard in a preclinical setting with a small-area detector was satisfying count-related specifications in the MWSR and SPECT reconstructed spatial resolution tests. For these tests, practical count-deprived acquisitions were obtained in favour of timely measurements as adherence to count criteria was inherently so time-consuming that it was considered unduly burdensome. One test that exceeded the count criteria was the intrinsic count rate performance in air which specifies that the final data point should be measured when the observed count rate drops below 4,000 cps because the dead time is only a fraction of a percent. Adherence to this specification would have yielded an overestimated 20% loss count rate of 10,000 cps due to a failure to extract the true input count rate from the linear response region of the detector.

Upon comparison with available reference values from Cubresa, the measured intrinsic spatial resolution of 0.851 ± 0.010 mm was in excellent agreement with the reference value of 0.85 mm. To our knowledge, this is the highest reported intrinsic

510 resolution of any γ-camera evaluated with the NEMA NU 1 standard to date. When

511 comparing the system sensitivities, measured results of 33.8 cps/MBq for the SPH

512 collimator and 150 cps/MBq for the MPH collimator were not in agreement with

513 the respective reference values of 50 cps/MBq and 467 cps/MBq. Instead, Cubresa's

514 reference sensitivities appear to relate to the overall console count rate before data

515 processing, which can be understood as follows: As the input count rate increases

516 linearly, the overall console count rate also increases proportionally, but the observed

517 count rate does not. In the linear region of the count rate performance curve at low

518 input count rates, the overall console count rate was approximately $1.65\times$ greater

519 than the observed count rate. However, it increased exponentially to $3.81\times$ at the

520 maximum observed count rate. This range of multiplicative factors is consistent with

521 Cubresa's reference sensitivities when applied to the NEMA sensitivity results.

522 When comparing internal results between measurement and simulation, the intrin-

523 sic performance parameters were very similar, and measured results were accurately

524 simulated, which primarily validates the GATE detector head and digitizer settings.

525 The parameters set in the digitizer differ from the corresponding observables, high-

526 lighting the importance of tuning the digitizer — a complex achievement with the

527 Spark since it is not a conventional γ-camera. This process was made simpler and

528 more accurate by applying NEMA's methodology. Comparisons of the system and

529 SPECT performance also showed excellent agreement between measurement and

530 simulation, with the most considerable differences amounting to $\lesssim 7\%$. Altogether,

531 these results confirm the accuracy of the Monte Carlo simulation results and sat-

532 isfy the secondary objective of validating the GATE simulation model of the Spark

533 for future use in preclinical SPECT studies, such as validating STIR's forthcoming

534 pinhole-SPECT image reconstruction capabilities.

535 When tuning the GATE model for the system and tomographic simulations, a

536 0.85 mm pinhole diameter was defined for the SPH collimator to better match

the measured and simulated collimator-detector response functions in terms of resolution and sensitivity. Using a 1.0 mm-diameter pinhole, the simulated system resolution without scatter was characterized as FWHM $= 0.0424D + 1.12$ (mm), which agrees well with theoretical equations from Van Audenhaege et al. [29], but predicts a limiting resolution of 2.10 mm at the center of rotation that does not correspond with the measured result of 1.87 mm. This discrepancy can be attributed to a vendor-specific event positioning algorithm that improves the Spark's resolution, which could not be accounted for using the digitizer. Similarly, the simulated 1.0 mm pinhole system planar sensitivity was characterized as $S_{\mathrm{TOT}} = 4.33 + 148\mathrm{e}^{(-0.0563D)}$ (cps/MBq), which predicts a sensitivity of 44.9 cps/MBq at the center of rotation which is much greater than the measured result of 33.8 cps/Mbq. This discrepancy could relate to the choice of G4_CESIUM_IODIDE as the scintillator material from the Geant4 database. This predefined material describes unactivated CsI and has the same physical characteristics as CsI(Na) and thallium-activated CsI (CsI(Tl)), but differs in terms of optical properties such as scintillation light yield, de-excitation time, refractive index, and peak emission wavelength [30, 31]. The introduction of optical properties into the simulation could allow for simulation of the entire SiPM readout logic to improve sensitivity and overall simulation accuracy. However, it would significantly increase computation time. Current efforts are ongoing to incorporate SiPM-specific software into GATE's digitizer to reproduce signals from SiPMs [32, 33].

Several commercially available preclinical SPECT systems have been validated with GATE using ^{99m}Tc and are compared in Table 7. Comparisons with pinhole collimators are made against 1.0 mm-diameter pinholes where data were available except for the NanoSPECT/CT$^{\mathrm{PLUS}}$ which uses 1.5 mm pinholes. System and SPECT parameters are cited at the radius of rotation. These tabulated studies not only demonstrate the flexibility and reliability of GATE for accurately modelling

564 various detector designs but also illustrate the potential of SiPMs in molecular

565 imaging. Comparisons of γ-camera performance for different imaging systems are

566 best performed according to the NEMA NU 1 standard as it provides a uniform and

567 consistent method for measuring and reporting performance parameters for various

568 camera designs. Unfortunately, most tabulated systems were not evaluated with

569 NEMA standards, perhaps due to the absence of a dedicated preclinical SPECT

570 standard from NEMA, a shortage of required resources, or a restriction from es-

571 sential scanner data. Therefore, direct comparisons are limited due to inconsistent

572 reporting parameters from different researchers and organizations. Nonetheless, this

573 study has demonstrated competitive performance characteristics of the novel SiPM-

574 based SPECT system, including the highest intrinsic spatial resolution of the tabu-

575 lated γ-cameras, the smallest form factor, good energy resolution, and comparable

576 sensitivity and tomographic resolution to the top-performing preclinical systems.

Table 7 Performance characteristic comparisons of commercial preclinical SPECT cameras validated with GATE.

Reporting parameter	Spark	X-SPECT	Inveon	HiReSPECT	NanoSPECT
Detection method	SiPM	CZT	PSPMT	PSPMT	PMT
Scintillator[3]	CsI(Na)	N/A	NaI(Tl)	CsI(Na)	NaI(Tl)
Collimator[4]	SPH/MPH	SPH/MPH	SPH/MPH	PH	SPH/MPH
Radius of rotation (mm)	28	25	25	25	45
Magnification factor	~1×	~4×	~4×	1×	~3.5×
Intrinsic spatial resolution (mm)	0.85	1.5	N/A	N/A	3.2
Intrinsic energy resolution (%)	14.7	5	12.4	19.15	9.7
System resolution (mm)	SPH: 1.87	SPH: 1.02	N/A	2.79	N/A
Sensitivity (cps/MBq)	SPH: 34 MPH: 150	MPH: 155	SPH: 38 MPH: 286	36 - 42	SPH: 42 MPH: 191
SPECT resolution (mm)	SPH: 1.37 MPH: 1.19	MPH: 0.58	SPH: 1.25	1.7	SPH: 1.27 MPH: 1.24
References	N/A	[9, 34, 35]	[10, 36, 37]	[11, 38, 39]	[12]

[3]SPH: Single-pinhole, MPH: Multi-pinhole, PH: Parallel-hole
[4]CsI(Na): Sodium-activated cesium iodide, NaI(Tl): Thallium-activated sodium iodide
N/A: Not applicable or not available

Conclusion

578 The performance of a novel, preclinical SiPM-based SPECT scanner has been char-

579 acterized according to the NEMA NU 1-2018 Standard for Performance Measure-

580 ments of Gamma Cameras. Measured and simulated NEMA tests were highly com-

581 parable, where the most considerable differences were below 7%, and overall dif-

582 ferences were a few percent. This confirms simulation accuracy and satisfies the

583 secondary objective of validating the GATE Monte Carlo model. The multi-pinhole

584 collimator investigated in this study offers the optimal combination of spatial res-

585 olution and sensitivity for organ-specific imaging of small animals, and the single-

586 pinhole collimator enables high-resolution whole-body imaging of small animals.

587 This work demonstrates that a SiPM detector mitigates the need for highly mag-

588 nifying collimators while preserving detailed information in projection images.

Declarations
589

Abbreviations
598

599 3D: Three-dimensional; ^{57}Co: Cobalt-57; ^{67}Ga: Gallium-67; ^{99m}Tc: Technetium-99m; CsI(Na):

600 Sodium-activated cesium iodide; CsI(Tl): Thallium-activated cesium iodide; CT: computed tomography; CZT:

601 Cadmium zinc telluride; EGS: Electron Gamma Shower; FBP: Filtered back projection; FOV: Field of view;

602 FWHM: Full width at half maximum; FWTM: Full width at tenth maximum; GATE: Geant4 Application for

603 Tomographic Emission; Geant4: Geometry and Tracking; ICR: Input count rate; LSF: Line spread functions;

604 Meas: Measurement; MLEM: Maximum likelihood expectation maximization; MCNP: Monte Carlo N-Particle;

605 MPH: Multi-pinhole; MWSR: Multiple window spatial registration; NaI(Tl): Thallium-activated sodium iodide;

606 NEMA: National Electrical Manufacturers Association; OCR: Observed count rate; PET: Positron emission

607 tomography; PH: Parallel-hole; PMT: Photomultiplier tube; PSF: Point spread function; PSPMT: Position

608 sensitive photomultiplier tube; RMS: Root-mean-square; ROI: Region of interest; Sim: Simulation; ROOT:

609 Rapid Objected-Oriented Technology; SiPM: Silicon-photomultiplier; SPECT: Single-photon emission computed

610 tomography; SPH: Single-pinhole; STIR: Software for Tomographic Image Reconstruction; STL: Standard

611 tessellation language; SVS: System volume sensitivity; UFOV: Useful field of view; VOI: Volume of interest;

612 VSAC: Volume sensitivity per axial centimeter.

Availability of data and materials
613

614 The datasets used and/or analyzed during the current study are available from the corresponding author on

615 reasonable request.

Ethics approval and consent to participate

Not applicable.

Competing interests

The Biomedical Translational Imaging Centre and Cubresa share an academic-industry research collaboration.

Consent for publication

Not applicable.

Authors' contributions

MS performed data collection and analysis and wrote the manuscript. DD, SB, and KB contributed to the conceptualization and review of the study. All authors contributed to the revision of the manuscript and read and approved the final draft.

Author details

[1]Biomedical Translational Imaging Centre, Halifax, NS, Canada. [2]Department of Physics and Atmospheric Science, Dalhousie University, Halifax, NS, Canada. [3]Cubresa Inc., Winnipeg, MB, Canada. [4]Department of Diagnostic Radiology, Dalhousie University, Halifax, NS, Canada. [5]School of Biomedical Engineering, Dalhousie University, Halifax, NS, Canada. [6]Department of Microbiology and Immunology, Dalhousie University, Halifax, NS, Canada.

References

1. Marquis, H., Deidda, D., Gillman, A., Willowson, K.P., Gholami, Y., Hioki, T., Eslick, E., Thielemans, K., Bailey, D.L.: Theranostic SPECT reconstruction for improved resolution: application to radionuclide therapy dosimetry. EJNMMI Physics **8**(1), 16 (2021). doi:10.1186/s40658-021-00362-x

2. Alves, R.R.N., Policarpo, I.d.S.: Animals and Human Health: Where Do They Meet? In: Ethnozoology, pp. 233–259. Elsevier, London (2018). doi:10.1016/B978-0-12-809913-1.00013-2. https://linkinghub.elsevier.com/retrieve/pii/B9780128099131000132

3. Franc, B.L., Acton, P.D., Mari, C., Hasegawa, B.H.: Small-Animal SPECT and SPECT/CT: Important Tools for Preclinical Investigation. Journal of Nuclear Medicine **49**(10), 1651–1663 (2008). doi:10.2967/jnumed.108.055442

4. Cunha, L., Horvath, I., Ferreira, S., Lemos, J., Costa, P., Vieira, D., Veres, D.S., Szigeti, K., Summavielle, T., Máthé, D., Metello, L.F.: Preclinical imaging: an essential ally in modern biosciences. Molecular Diagnosis & Therapy **18**(2), 153–173 (2014). doi:10.1007/s40291-013-0062-3

5. Sarrut, D., Bała, M., Bardiès, M., Bert, J., Chauvin, M., Chatzipapas, K., Dupont, M., Etxebeste, A., M Fanchon, L., Jan, S., Kayal, G., S Kirov, A., Kowalski, P., Krzemien, W., Labour, J., Lenz, M., Loudos, G., Mehadji, B., Ménard, L., Morel, C., Papadimitroulas, P., Rafecas, M., Salvadori, J., Seiter, D., Stockhoff, M., Testa, E., Trigila, C., Pietrzyk, U., Vandenberghe, S., Verdier, M.-A., Visvikis, D., Ziemons, K., Zvolský, M., Roncali, E.: Advanced Monte Carlo simulations of emission tomography imaging systems with GATE. Physics in Medicine & Biology **66**(10), 10–03 (2021). doi:10.1088/1361-6560/abf276

6. Allison, J., Amako, K., Apostolakis, J., Arce, P., Asai, M., Aso, T., Bagli, E., Bagulya, A., Banerjee, S., Barrand, G., Beck, B.R., Bogdanov, A.G., Brandt, D., Brown, J.M.C., Burkhardt, H., Canal, P., Cano-Ott, D., Chauvie, S., Cho, K., Cirrone, G.A.P., Cooperman, G., Cortés-Giraldo, M.A., Cosmo, G., Cuttone, G., Depaola, G., Desorgher, L., Dong, X., Dotti, A., Elvira, V.D., Folger, G., Francis, Z., Galoyan, A., Garnier, L., Gayer, M., Genser, K.L., Grichine, V.M., Guatelli, S., Guèye, P., Gumplinger, P., Howard, A.S., Hřivnáčová, I., Hwang, S., Incerti, S., Ivanchenko, A., Ivanchenko, V.N., Jones, F.W., Jun, S.Y.,
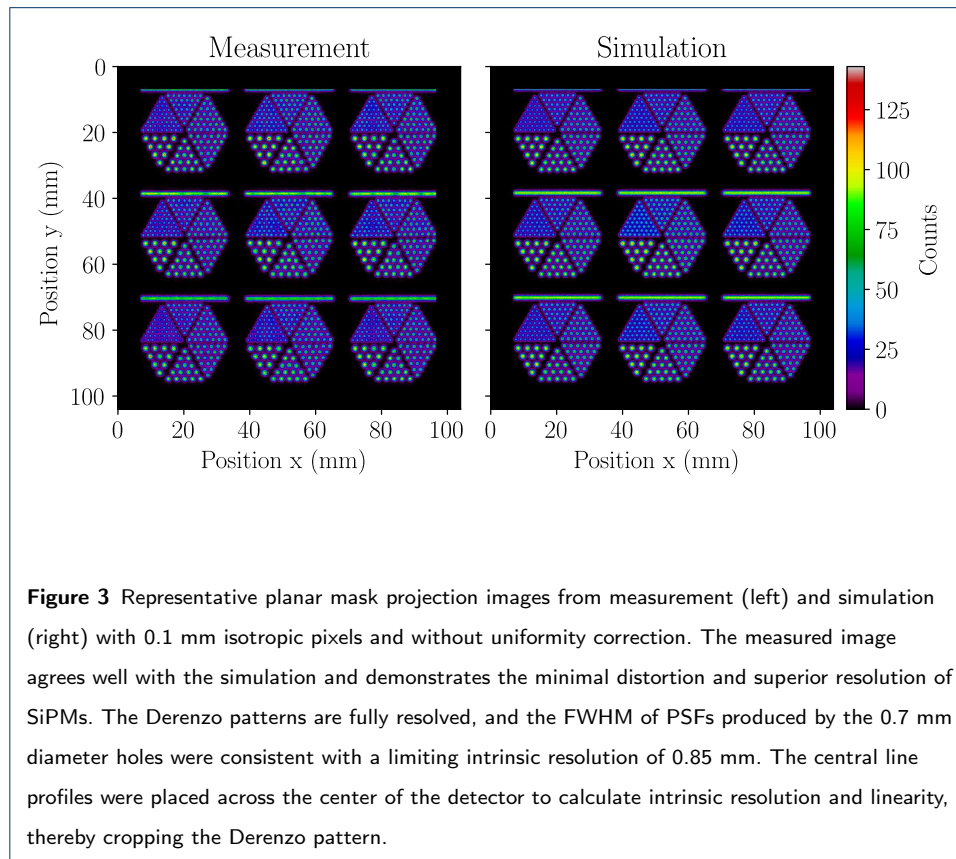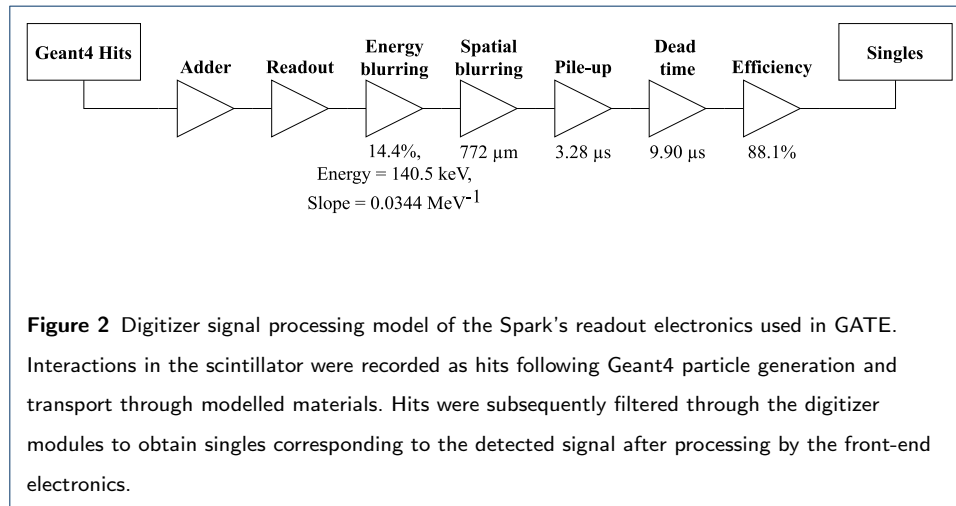
657 Kaitaniemi, P., Karakatsanis, N., Karamitros, M., Kelsey, M., Kimura, A., Koi, T., Kurashige, H., Lechner,

658 A., Lee, S.B., Longo, F., Maire, M., Mancusi, D., Mantero, A., Mendoza, E., Morgan, B., Murakami, K.,

659 Nikitina, T., Pandola, L., Paprocki, P., Perl, J., Petrović, I., Pia, M.G., Pokorski, W., Quesada, J.M.,

660 Raine, M., Reis, M.A., Ribon, A., Ristić Fira, A., Romano, F., Russo, G., Santin, G., Sasaki, T., Sawkey,

661 D., Shin, J.I., Strakovsky, I.I., Taborda, A., Tanaka, S., Tomé, B., Toshito, T., Tran, H.N., Truscott, P.R.,

662 Urban, L., Uzhinsky, V., Verbeke, J.M., Verderi, M., Wendt, B.L., Wenzel, H., Wright, D.H., Wright,

663 D.M., Yamashita, T., Yarba, J., Yoshida, H.: Recent developments in Geant4. Nuclear Instruments and

664 Methods in Physics Research Section A: Accelerators, Spectrometers, Detectors and Associated Equipment

665 **835**, 186–225 (2016). doi:10.1016/j.nima.2016.06.125

666 7. Kawrakow, I., Rogers, D.W.O., Mainegra-Hing, E., Tessier, F., Townson, R.W., Walters, B.R.B.: EGSnrc

667 toolkit for Monte Carlo simulation of ionizing radiation transport. National Research Council of Canada

668 (2000). doi:10.4224/40001303. https://github.com/nrc-cnrc/EGSnrc Accessed 2022-04-06

669 8. Werner, C.J., Bull, J.S., Solomon, C.J., Brown, F.B., McKinney, G.W., Rising, M.E., Dixon, D.A., Martz,

670 R.L., Hughes, H.G., Cox, L.J., Zukaitis, A.J., Armstrong, J.C., Forster, R.A., Casswell, L.: MCNP Version

671 6.2 Release Notes. Technical Report LA-UR–18-20808, 1419730 (February 2018). doi:10.2172/1419730.

672 http://www.osti.gov/servlets/purl/1419730/ Accessed 2022-04-06

673 9. Mok, G.S.P., Du, Y., Wang, Y., Frey, E.C., Tsui, B.M.W.: Development and Validation of a Monte Carlo

674 Simulation Tool for Multi-Pinhole SPECT. Molecular Imaging and Biology **12**(3), 295–304 (2010).

675 doi:10.1007/s11307-009-0263-7

676 10. Lee, S.-h., Gregor, J., Kennel, S.J., Osborne, D.R., Wall, J.: GATE Validation of Standard Dual Energy

677 Corrections in Small Animal SPECT-CT. PLOS ONE **10**(4) (2015). doi:10.1371/journal.pone.0122780

678 11. Sadremomtaz, A., Telikani, Z.: Validation and optimization studies of small animal SPECT using GATE

679 Monte Carlo simulation. Nuclear Instruments and Methods in Physics Research Section A: Accelerators,

680 Spectrometers, Detectors and Associated Equipment **915**, 94–101 (2019). doi:10.1016/j.nima.2018.09.068

681 12. Lukas, M., Kluge, A., Beindorff, N., Brenner, W.: Accurate Monte Carlo Modeling of Small-Animal

682 Multi-Pinhole SPECT for Non-Standard Multi-Isotope Applications. IEEE Transactions on Medical

683 Imaging **40**(9), 2208–2220 (2021). doi:10.1109/TMI.2021.3073749

684 13. Jiang, W., Chalich, Y., Deen, M.J.: Sensors for Positron Emission Tomography Applications. Sensors

685 **19**(22), 5019 (2019). doi:10.3390/s19225019

686 14. DeBay, D.R., Reid, G.A., Pottie, I.R., Martin, E., Bowen, C.V., Darvesh, S.: Targeting

687 butyrylcholinesterase for preclinical single photon emission computed tomography (SPECT) imaging of

688 Alzheimer's disease. Alzheimer's & Dementia: Translational Research & Clinical Interventions **3**(2),

689 166–176 (2017). doi:10.1016/j.trci.2017.01.005

690 15. NEMA Standards Publication NU 1-2018, Performance Measurements of Gamma Cameras. National

691 Electrical Manufacturers Association (2019)

692 16. Bal, G., Acton, P.D.: Analytical derivation of the point spread function for pinhole collimators. Physics in

693 Medicine and Biology **51**(19), 4923–4950 (2006). doi:10.1088/0031-9155/51/19/013

694 17. Strugari, M., Falcon, C., Erlandsson, K., Hutton, B.F., Reid, G.A., Pottie, I.R., Darvesh, S., Beyea, S.,

695 Brewer, K.D., Thielemans, K.: Integration of advanced 3D SPECT modelling for pinhole collimators into

696 the open-source STIR framework. In: 2022 IEEE Nuclear Science Symposium and Medical Imaging

697 Conference (NSS/MIC), pp. 1–2. IEEE, Milan, Italy (2022)

698 18. Thielemans, K., Tsoumpas, C., Mustafovic, S., Beisel, T., Aguiar, P., Dikaios, N., Jacobson, M.W.: STIR:

699 software for tomographic image reconstruction release 2. Physics in Medicine and Biology **57**(4), 867–883

700   (2012). doi:10.1088/0031-9155/57/4/867

701   19.   Fuster, B.M., Falcon, C., Tsoumpas, C., Livieratos, L., Aguiar, P., Cot, A., Ros, D., Thielemans, K.:

702   Integration of advanced 3D SPECT modeling into the open-source STIR framework: SPECT

703   reconstruction with STIR. Medical Physics **40**(9), 092502 (2013). doi:10.1118/1.4816676

704   20.   Beque, D., Nuyts, J., Bormans, G., Suetens, P., Dupont, P.: Characterization of pinhole SPECT acquisition

705   geometry. IEEE Transactions on Medical Imaging **22**(5), 599–612 (2003). doi:10.1109/TMI.2003.812258

706   21.   Beque, D., Nuyts, J., Suetens, P., Bormans, G.: Optimization of geometrical calibration in pinhole SPECT.

707   IEEE Transactions on Medical Imaging **24**(2), 180–190 (2005). doi:10.1109/TMI.2004.839367

708   22.   Brun, R., Rademakers, F.: ROOT — An object oriented data analysis framework. Nuclear Instruments and

709   Methods in Physics Research Section A: Accelerators, Spectrometers, Detectors and Associated Equipment

710   **389**(1-2), 81–86 (1997). doi:10.1016/S0168-9002(97)00048-X

711   23.   Bé, M.-M., Chisté, V., Dulieu, C., Kellett, M., Mougeot, X., Arzu, A., Chechev, V., Kuzmenko, N., Kibédi,

712   T., Luca, A., Nichols, A.: Table of Radionuclides. Monographie BIPM, vol. 8. Bureau International des

713   Poids et Mesures, Pavillon de Breteuil, F-92310 Sèvres, France (2016). OCLC: 935014645

714   24.   Radiation Solutions Inc.: Pulse Pile-up and Pile-up Rejection.

715   https://www.radiationsolutions.ca/fileadmin/pdf/Pulse_Pile-up.pdf Accessed 2021-10-20

716   25.   Knoll, G.F.: Radiation Detection and Measurement, 4th edn. John Wiley, Hoboken, N.J (2010). OCLC:

717   ocn612350364

718   26.   Hutton, B.F., Buvat, I., Beekman, F.J.: Review and current status of SPECT scatter correction. Physics in

719   Medicine and Biology **56**(14), 85–112 (2011). doi:10.1088/0031-9155/56/14/R01

720   27.   NEMA Standards Publication NU 4-2008, Performance Measurements of Small Animal Positron Emission

721   Tomographs (PETs). National Electrical Manufacturers Association (2008). https://www.nema.org/

722   standards/view/Performance-Measurements-of-Small-Animal-Positron-Emission-Tomographs

723   28.   Graham, L.S., Fahey, F.H., Madsen, M.T., van Aswegen, A., Yester, M.V.: Quantitation of SPECT

724   performance: Report of Task Group 4, Nuclear Medicine Committee. Medical Physics **22**(4), 401–409

725   (1995). doi:10.1118/1.597605

726   29.   Van Audenhaege, K., Van Holen, R., Vandenberghe, S., Vanhove, C., Metzler, S.D., Moore, S.C.: Review

727   of SPECT collimator selection, optimization, and fabrication for clinical and preclinical imaging. Medical

728   Physics **42**(8), 4796–4813 (2015). doi:10.1118/1.4927061

729   30.   Saint-Gobain Ceramics and Plastics, Inc.: CsI(Tl), CsI(Na), Cesium Iodide Scintillation Material (2012).

730   https://www.gammadata.se/assets/Uploads/CsITl-and-Na-data-sheet.pdf Accessed 2022-01-12

731   31.   Gupta, T.: Radiation, Ionization, and Detection in Nuclear Medicine. Springer, Heidelberg (2013)

732   32.   Mehadji, B.: Modélisation Monte Carlo d'une caméra Compton basée sur l'utilisation de détecteurs à

733   scintillation sensibles à la position couplés à des SiPM. Ph.D. Thesis, Aix-Marseille University, Marseille,

734   France (May 2021). https://www.theses.fr/2021AIXM0212.pdf Accessed 2022-02-23

735   33.   Lenz, M.: Design and Characterisation of an MRI Compatible Human Brain PET Insert by Means of

736   Simulation and Experimental Studies. Ph.D. Dissertation, Bergische Universität Wuppertal, Wuppertal,

737   Germany (2020). Publisher: Bergische Universität Wuppertal.

738   http://elpub.bib.uni-wuppertal.de/servlets/DocumentServlet?id=11590 Accessed 2022-02-23

739   34.   Larsson Åkerman, L.: A technical validation of the PET/SPECT/CT (Triumph) scanner. Ph.D. Thesis,

740   Uppsala University, Uppsala, Sweden (February 2011).

741   http://www.diva-portal.org/smash/get/diva2:407708/FULLTEXT01.pdf Accessed 2022-02-24

742   35.   Deleye, S., Van Holen, R., Verhaeghe, J., Vandenberghe, S., Stroobants, S., Staelens, S.: Performance
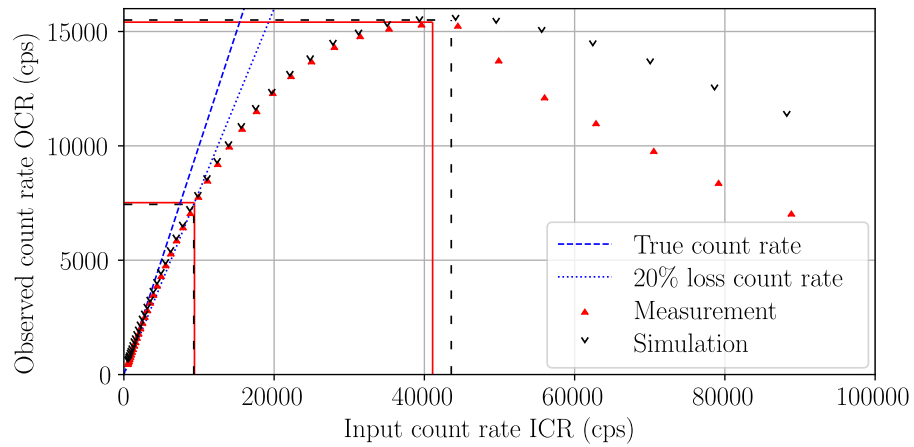
743   evaluation of small-animal multipinhole μSPECT scanners for mouse imaging. European Journal of Nuclear

744   Medicine and Molecular Imaging **40**(5), 744–758 (2013). doi:10.1007/s00259-012-2326-2

745   36. Lee, S.-h., Gregor, J., Osborne, D.R.: Initial validation of a complete GATE model of the Siemens Inveon

746   trimodal imaging system. In: 2012 IEEE Nuclear Science Symposium and Medical Imaging Conference

747   Record (NSS/MIC), pp. 2540–2542. IEEE, Anaheim, CA, USA (2012).

748   doi:10.1109/NSSMIC.2012.6551580. http://ieeexplore.ieee.org/document/6551580/

749   37. Boisson, F., Zahra, D., Parmar, A., Gregoire, M.-C., Meikle, S.R., Hamse, H., Reilhac, A.: Imaging

750   Capabilities of the Inveon SPECT System Using Single-and Multipinhole Collimators. Journal of Nuclear

751   Medicine **54**(10), 1833–1840 (2013). doi:10.2967/jnumed.112.117572

752   38. Sajedi, S., Zeraatkar, N., Moji, V., Farahani, M.H., Sarkar, S., Arabi, H., Teymoorian, B., Ghafarian, P.,

753   Rahmim, A., Reza Ay, M.: Design and development of a high resolution animal SPECT scanner dedicated

754   for rat and mouse imaging. Nuclear Instruments and Methods in Physics Research Section A: Accelerators,

755   Spectrometers, Detectors and Associated Equipment **741**, 169–176 (2014).

756   doi:10.1016/j.nima.2014.01.001

757   39. Moji, V., Zeraatkar, N., Farahani, M.H., Aghamiri, M.R., Sajedi, S., Teimourian, B., Ghafarian, P., Sarkar,

758   S., Ay, M.R.: Performance evaluation of a newly developed high-resolution, dual-head animal SPECT

759   system based on the NEMA NU1-2007 standard. Journal of Applied Clinical Medical Physics **15**(6),

760   267–278 (2014). doi:10.1120/jacmp.v15i6.4936

761   **Figures**

Figure 1 The Spark preclinical SPECT scanner illustrated in a cutaway side view of the manufacturer's model (left) and GATE model (right). Only the detector head and single-pinhole collimator were included in the Monte Carlo model.

Figure 2 Digitizer signal processing model of the Spark's readout electronics used in GATE. Interactions in the scintillator were recorded as hits following Geant4 particle generation and transport through modelled materials. Hits were subsequently filtered through the digitizer modules to obtain singles corresponding to the detected signal after processing by the front-end electronics.

Figure 3 Representative planar mask projection images from measurement (left) and simulation (right) with 0.1 mm isotropic pixels and without uniformity correction. The measured image agrees well with the simulation and demonstrates the minimal distortion and superior resolution of SiPMs. The Derenzo patterns are fully resolved, and the FWHM of PSFs produced by the 0.7 mm diameter holes were consistent with a limiting intrinsic resolution of 0.85 mm. The central line profiles were placed across the center of the detector to calculate intrinsic resolution and linearity, thereby cropping the Derenzo pattern.

Figure 4 Intrinsic count rate performance in air. Measured results are shown with red solid carets and simulated results with black empty carets. Additional lines illustrate the maximum OCR and 20% loss OCR for measurement (solid lines) and simulation (dashed lines). The count rates are in agreement below the maximum OCR while above the maximum, the measured OCR falls off the trend line as the photopeak shifted to lower energies.
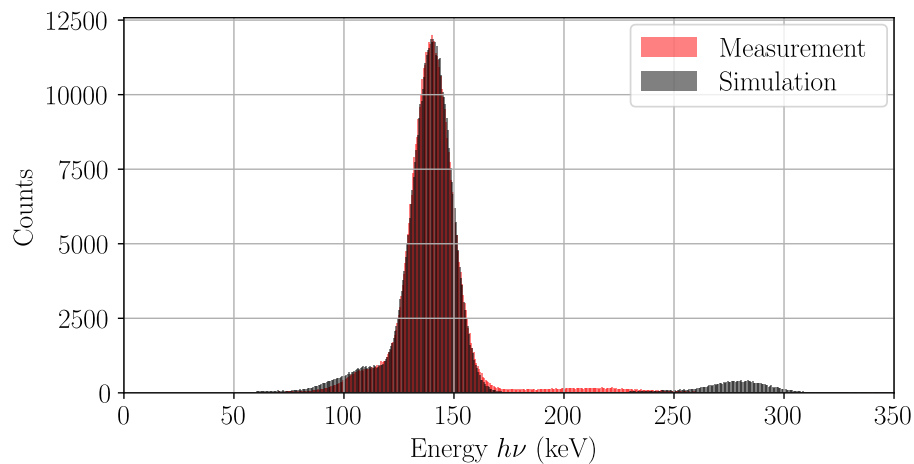

Figure 5 Measured and simulated ^{99m}Tc energy spectra acquired at a count rate loss below 20%. The intrinsic resolution was 14.7% in both cases. Differences can be observed in the pile-up energy distribution due to partial scintillation light collection of the SiPM array, which was not modelled with GATE.
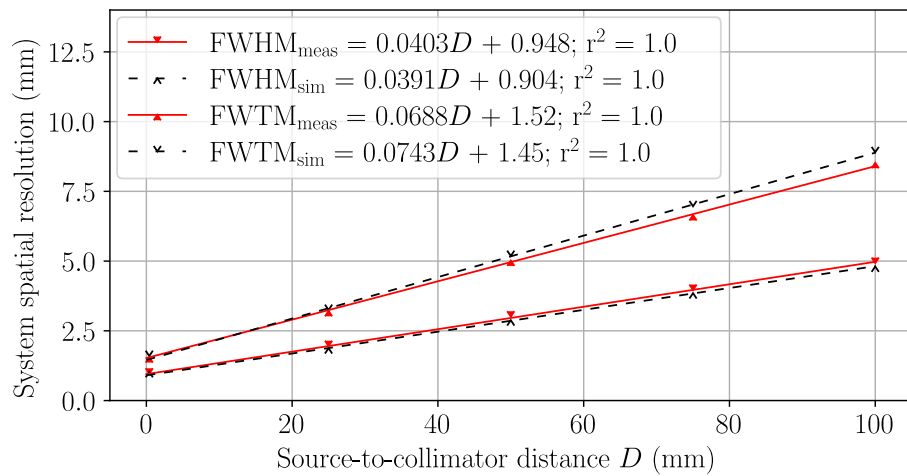
Figure 6 System spatial resolution without scatter presented in terms of FWHM and FWTM for the SPH collimator. Measured results are shown with solid red carets and solid lines of best fit, and simulated results are shown with empty black carets and dashed lines of best fit. Equations for lines of best fit are distinguished in the legend with abbreviated subscripts. The measured (simulated) system resolution without scatter at the center of rotation was 1.87 mm (1.80 mm).
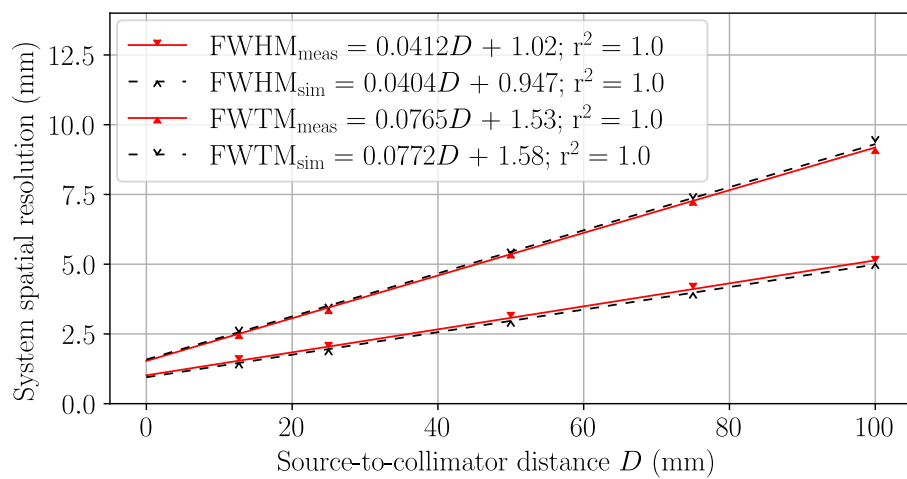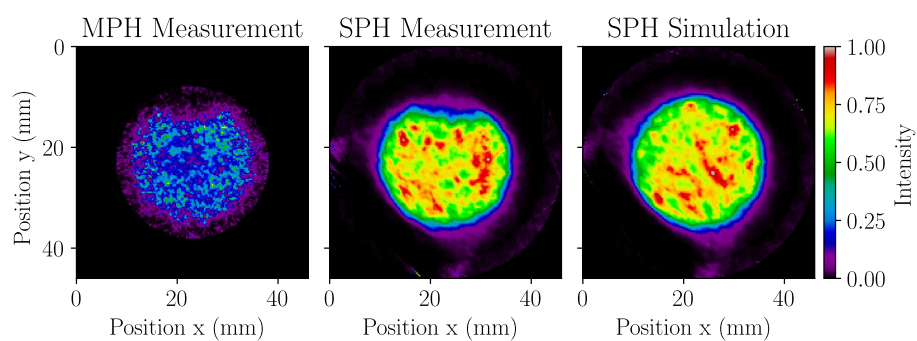

Figure 7 System spatial resolution with scatter in a custom mouse phantom presented in terms of FWHM and FWTM for the SPH collimator. Measured results are shown with solid red carets and solid lines of best fit, and simulated results are shown with empty black carets and dashed lines of best fit. Equations for lines of best fit are distinguished in the legend with abbreviated subscripts. The measured (simulated) system resolution with scatter at the center of rotation was 1.97 mm (1.88 mm).
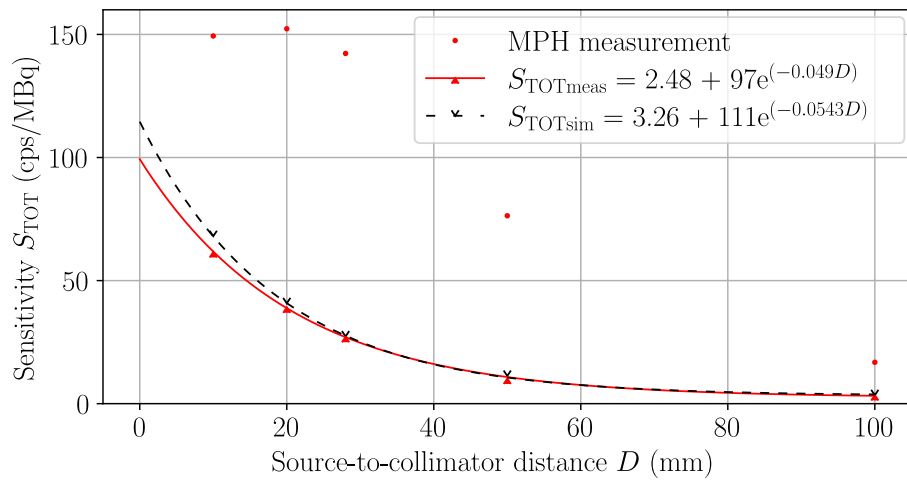
Figure 8 Planar sensitivity as a function of source-to-collimator distance. For the SPH collimator, measured results are shown with solid red carets, and a solid line of best fit and simulated results are shown with black with empty carets and a dashed line of best fit. MPH collimator results are shown as red dots. Fit equations for the SPH collimator measurement and simulation are distinguished in the legend with abbreviated subscripts. The MPH collimator geometry is optimized for increased sensitivity in the tomographic FOV, whereas the SPH collimator sensitivity increases when approaching the pinhole.
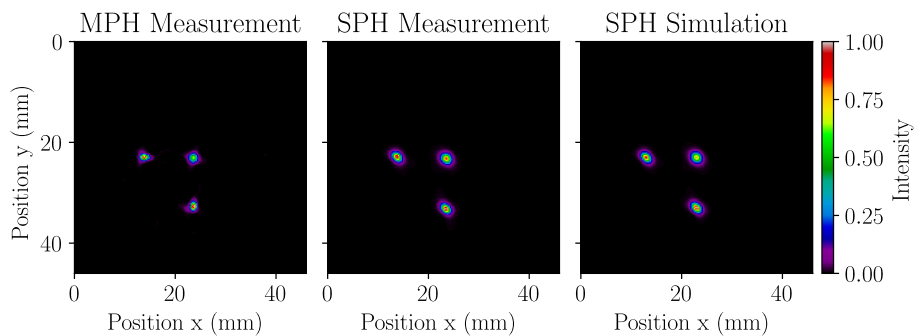
Figure 9 SPECT reconstructed spatial resolution with scatter evaluated with a custom mouse phantom in MPH collimator measurement (left), SPH collimator measurement (middle), and SPH collimator simulation (right). The images present the central 3.5 mm-thick transverse slice used in calculating the radial, tangential, and central resolution. The MPH collimator offers superior tomographic resolution compared to the SPH collimator when scanning relatively small radioactivity distributions.

1
2
3
4
5
6
7
8
9
10
11
12
13
14
15
16
17
18
19
20
21
22
23
24
25
26
27
28
29
30
31
32
33
34
35
36
37
38
39
40
41
42
43
44
45
46
47
48
49
50
51
52
53
54
55
56
57
58
59
60
61
62
63
64
65

Figure 10 SPECT volume sensitivity and uniformity evaluated with a cylindrical phantom in MPH collimator measurement (left), SPH collimator measurement (middle), and SPH collimator simulation (right). The images present the central 0.25 mm-thick transverse slice used in calculating volume uniformity and RMS noise. A bubble can be seen in the measured data that was not modelled in the simulation. The SPH collimator offers a larger FOV with superior uniformity and noise characteristics compared to the MPH collimator when scanning relatively large radioactivity distributions.

Reference PDF

Click here to access/download
Supplementary Material
Reference PDF.pdf